

Strategy for Direct Detection of Chiral Phonons with Phase-Structured Free Electrons

Marc R. Bourgeois,¹ Andrew W. Rossi,¹ and David J. Masiello^{1,*}

¹*Department of Chemistry, University of Washington, Seattle WA, 98195*

Chiral phonons possessing valley pseudo angular momentum (PAM) underlie a diversity of quantum phenomena of fundamental and applied importance, but are challenging to probe directly. We show that deficiencies of typical momentum-resolved electron energy loss measurements that make it impossible to distinguish the PAM of chiral phonons can be overcome by introducing pinwheel free electron states with well-defined PAM. Transitions between such states generate 2D periodic arrays of in-plane field vortices with polarization textures tailored to selectively couple to desired chiral mode symmetries.

Chirality plays a central role in nearly all aspects of physics, chemistry, and biology. At large length scales, chiral gravitational waves have been considered as sources of circularly polarized contributions to the cosmic microwave background [1], while at short length scales chirality dictates molecular interactions and organizations underpinning biological processes. In condensed matter physics, chirality and spin-momentum locking are at the heart of the menagerie of identified Hall effects, as well as stable [2, 3] and transient free space [4, 5] and evanescent [6–10] topological electromagnetic field textures. Following the report [11] of helicity-resolved Raman scattering experiments from transition-metal dichalcogenide (TMD) atomic layers, it was predicted [12] that two-dimensional (2D) atomic crystals with hexagonal symmetry can host chiral phonons with well-defined pseudo angular momentum (PAM) arising from discrete rotational crystal symmetry. Direct experimental evidence of chiral phonons was subsequently reported based on transient infrared circular dichroism measurements of a monolayer TMD [13], generating significant interest in the potential for leveraging chiral phonons to achieve novel material properties that are sensitive to low-energy spin-selective excitations. Beyond 2D hexagonal lattices, chiral phonons have been identified in other 2D [14–19] and 3D [20, 21] crystalline systems, as well as in bio-organic molecules [22]. Chiral phonons have also been recently identified as participants in various exotic condensed matter processes including anomalous thermal Hall conductivity [23] and the chiral-phonon-activated spin Seebeck effect [24], among others [25, 26]. Despite the high-level of current interest in chiral phonons, their experimental detection has been largely limited to optical Raman scattering measurements, with spatial resolution and linear momentum limited by the photon wavelength, and direct detection remains an outstanding challenge impeding further progress [27].

Meanwhile, instrumental advances during the past decade in aberration correction, monochromation, and detector technologies have made it possible to perform vibrational spectroscopy inside a scanning transmission electron microscope (STEM) [28–32]. In particular, momentum-resolved electron energy loss (q -EEL) spectroscopy [29, 33–35], and the related high-resolution EEL spectroscopy (HREELS) technique [36, 37], have been used to measure the energy-momentum dispersion of phonons in mono- and few-layer 2D atomic crystals. While these measurements have demonstrated the ability of inelastic free electron scattering to complement other phonon measurement techniques, such as inelastic neutron and x-ray scattering, the absence of an obvious electron polarization degree of freedom has hindered the spin-selective detection of chiral phonons using free electrons. However, the transverse phase shaping and

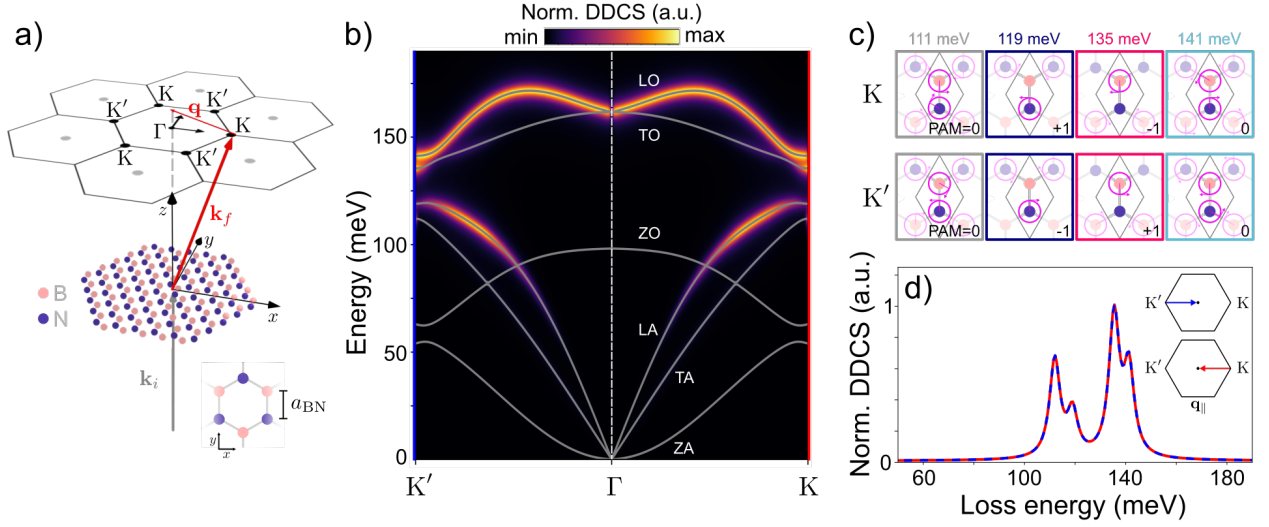


FIG. 1. hBN phonons and q -EEL spectroscopy. a) Scheme of q -EEL process involving momentum transfer between initial \mathbf{k}_i (gray) and final \mathbf{k}_f (red) free electron states. The recoil momentum $\hbar\mathbf{q}$ has projection $\mathbf{q}_{\parallel} = (\mathbf{q} \cdot \hat{\mathbf{x}})\hat{\mathbf{x}}$ onto the 2D sample situated in the xy plane. b) Calculated hBN phonon eigenmode dispersion (gray) along $K' \rightarrow \Gamma \rightarrow K$ and normalized DDSCS (color map). c) Real-space in-plane phonon eigenmodes at K and K' . Pink circles indicate circular motion of sublattices, while arrows show the direction of rotation. Integer PAM is noted in the lower-right of each panel. d) Lineouts of the DDSCS spectra at K and K' from panel (b). All calculations include an empirical damping rate of $\eta = 5$ meV/ \hbar at zero temperature and a vacuum background.

coherent detection schemes that were originally developed for core-loss EEL spectroscopy and that enabled magnetic circular dichroism measurements in the TEM [38–40] have been recently adapted to the low loss regime. By selectively monitoring inelastic scattering of free electrons between states with tailored transverse phase profiles, energy loss processes involving desired target mode symmetries [41] and OAM states [42, 43] have been demonstrated, and optical polarization analogs in free electron scattering have been identified [44, 45]. The full potential of these measurement schemes is currently being explored, while the transverse phase shaping and selection technologies underlying them are actively under development [46–50].

In this Letter we provide a strategy for leveraging inelastic scattering of transverse phase shaped free electrons to achieve direct detection of chiral phonons within a STEM. We introduce pinwheel free electron states composed of a small number of phased plane wave components that share the same reciprocal space three-fold discrete rotational symmetry as chiral phonons in hexagonal monolayer 2D atomic crystals at the K and K' points, which introduces a new PAM degree of freedom to the probing electrons. In analogy to previous work on OAM-resolved EEL spectroscopy [42–45, 51–53], pre- and post-selection of the transverse free electron states enables tracking of PAM exchange between pinwheel free electrons and the sample. We trace the utility of the identified phase-shaped free electron transitions to the topological spin textures of their associated transition electric fields, which can be tailored to selectively couple to chiral phonons of the same symmetry. Compared to light-based probes, inelastic electron scattering observables offer superior spatial resolution, in addition to an often simpler interpretation since the Brillouin zone (BZ) edges can be accessed directly. This work informs current and future efforts to detect and characterize chiral phonons using inelastic free electron scattering, and identifies specific experimental geometries and parameters to achieve detection.

As a model 2D atomic crystal with hexagonal symmetry, we consider chiral phonons in monolayer hexagonal boron

nitride (hBN) situated in the xy plane as depicted in Fig. 1a. Eigenenergies $\hbar\omega_\lambda(\mathbf{k}_\parallel)$ and eigenvectors $\boldsymbol{\xi}_\lambda(\mathbf{k}_\parallel)$ of the six hBN phonon bands, indexed by λ , are computed within the harmonic crystal approximation [54] with force constants taken from the literature [55–57]. The gray lines in Fig. 1b show the eigenenergies as a function of \mathbf{k}_\parallel within the first BZ along $K' \rightarrow \Gamma \rightarrow K$. In contrast to graphene, the lack of inversion symmetry within the 2D plane and the fact that time reversal symmetry is broken at the K and K' points leads to non-degenerate in-plane valley phonon modes at the K and K' reciprocal space points with well-defined PAM [12]. Real-space motion of the four in-plane phonon eigenmodes at the K and K' points are shown in Fig. 1c. The lowest and highest energy in-plane modes involve opposing circular motion of both sublattices, with total PAM = $0\hbar$. For the other two in-plane modes at 119 meV and 135 meV, while one sublattice remains motionless, the other executes circular motion, the handedness of which determines whether the PAM = $\pm 1\hbar$. The depicted phonons exhibit spin-momentum locking in that the z -oriented spin associated with each sublattice (equivalent to handedness of circular motion) changes sign under linear momentum reversal, i.e., $K \leftrightarrow K'$.

For an incoming probing electron with speed v_i , the state-resolved loss rate describing inelastic scattering at first order from the 2D atomic crystal at loss energy $\hbar\omega_{if}$ is [58]

$$w_{fi}^{\text{loss}} = \frac{2}{\hbar} \left(\frac{v_i}{L} \right)^2 \frac{L^3}{\Omega_0} \text{Im} \sum_{\lambda} \sum_{\mathbf{k}}^{\text{BZ}} \frac{|\tilde{\mathcal{F}}_{\lambda}(\mathbf{k})|^2}{\omega_{\lambda}^2 - \omega_{if}(\omega_{if} + i\eta)}, \quad (1)$$

where L^3 defines the probing electron's quantization volume, Ω_0 is the unit cell volume, and \mathbf{k} is within the first BZ. The quantity $\tilde{\mathcal{F}}_{\lambda}(\mathbf{k}) = \sum_{\mathbf{G}} \sum_{\kappa} \boldsymbol{\xi}_{\lambda\kappa}^* \cdot M_{\kappa}^{-1/2} \cdot e\bar{\mathbf{Z}}_{\kappa}(\mathbf{k} + \mathbf{G}) \cdot \mathbf{E}_{fi, \mathbf{k} + \mathbf{G}\kappa}^0$ involves the atomic masses M_{κ} and effective charges eZ_{κ} of each sublattice, indexed by κ , and \mathbf{G} denotes a reciprocal lattice vector. $\mathbf{E}_{fi, \mathbf{k} + \mathbf{G}\kappa}^0$ is the Fourier coefficient of the quasistatic transition electric field $\mathbf{E}_{fi}^0(\mathbf{k}) = -i\mathbf{k}(4\pi/k^2) \rho_{fi}(\mathbf{k})$, where $\rho_{fi}(\mathbf{k})$ is the Fourier transform of the charge density $\rho_{fi}(\mathbf{x}) = -e\psi_f^*(\mathbf{x})\psi_i(\mathbf{x})$ associated with the free electron transition from initial state $\psi_i(\mathbf{x})$ to final state $\psi_f(\mathbf{x})$. A phenomenological damping parameter η is introduced to give spectral features finite width. Fig. 1a shows a generic wide field inelastic electron scattering event as typically measured by q -EELS whereby an incoming free electron plane wave with wave vector \mathbf{k}_i (gray) scatters to an outgoing plane wave with wave vector \mathbf{k}_f (red) via interaction with the atomic crystal. In the low loss energy range considered, the linear momentum $\hbar\mathbf{q} = \hbar(\mathbf{k}_i - \mathbf{k}_f)$ lost by the probing electron is transferred into excited phonons with Bloch vector \mathbf{k}_\parallel . The transition field associated with this situation is

$$\mathbf{E}_{\mathbf{q}, \mathbf{k} + \mathbf{G}\kappa}^0 = \frac{4\pi ie}{L^3} \frac{L}{v_i} \frac{\mathbf{k} + \mathbf{G}}{|\mathbf{k} + \mathbf{G}|^2} e^{i(\mathbf{k} + \mathbf{G}) \cdot \mathbf{r}_{\kappa}} \delta_{\mathbf{k} + \mathbf{G}, \mathbf{q}}, \quad (2)$$

which is linearly polarized along the recoil direction $\hat{\mathbf{q}}$. The rate of phonon mode excitation is dictated by $\tilde{\mathcal{F}}_{\lambda}(\mathbf{q}) \propto \boldsymbol{\xi}_{\lambda\kappa}^* \cdot \mathbf{E}_{\mathbf{q}, \mathbf{k} + \mathbf{G}\kappa}^0 \propto \boldsymbol{\xi}_{\lambda\kappa}^* \cdot \hat{\mathbf{q}}$. As a consequence, the linearly polarized transition field couples identically to circularly polarized in-plane phonons, and it is not possible to distinguish the PAM of the phonon modes at K and K' points from q -EEL spectra alone. Indeed, spectral lineouts of the double differential cross section (DDCS) [59, 60] at the K and K' points from Fig. 1b are shown in Fig. 1d to be indistinguishable.

It is perhaps natural to consider employing prototypical free electron states that carry well-defined units of intrinsic

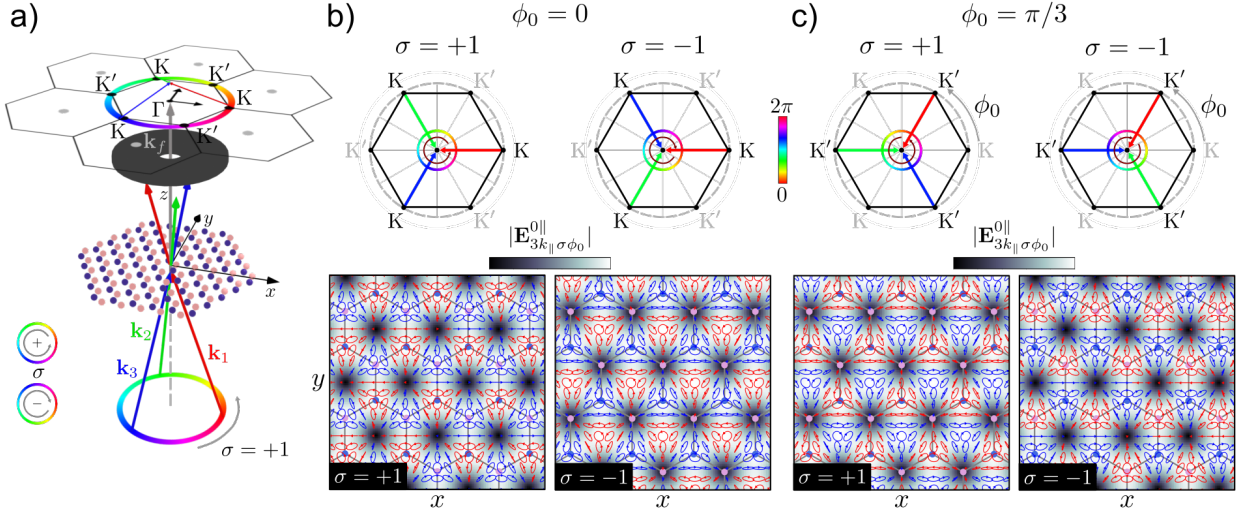


FIG. 2. Transition electric fields involving three-fold pinwheel states. a) Scheme showing a transition from the $|P=3, k_{\parallel}, \sigma = +1, \phi_0\rangle$ pinwheel state to $|\mathbf{k}_f^{\parallel} = \mathbf{0}\rangle$. b) and c) show in-plane magnitudes (color maps) and polarization textures (polarization ellipses) of $\mathbf{E}_{3k_{\parallel}\sigma\phi_0}^{(0)}(\mathbf{x}_{\parallel}, z=0)$ associated with transitions $|P=3, k_{\parallel} = K, \sigma = \pm 1, \phi_0\rangle \rightarrow |\mathbf{k}_f^{\parallel} = \mathbf{0}\rangle$ at $\phi_0 = 0$ and $\phi_0 = \pi/3$, respectively. Red (blue) polarization ellipses indicate anticlockwise (clockwise) elliptical polarization rotation, and $\mathbf{R}_0 = -a_{\text{BN}}/2$.

OAM, e.g., Bessel and Laguerre-Gauss beams [61–63]. Previous works have demonstrated the ability to monitor OAM exchange between target sample and probing electron through careful pre- and post-selection of the OAM state of the free electrons [42–45, 51–53]. However, this strategy is also problematic in the present case, since the reciprocal space wave function densities of these free electron states are azimuthally symmetric, leading to the inability to selectively probe the K or K' points. To circumvent this challenge, we introduce pinwheel initial states $|P k_{\parallel} \sigma \phi_0\rangle$ of the free electron probe defined as

$$\psi_{P k_{\parallel} \sigma \phi_0}(\mathbf{x}) = \frac{1}{\sqrt{P}} \sum_{j=1}^P e^{i\phi_j} L^{-3/2} e^{i\mathbf{k}_j \cdot \mathbf{x}}, \quad (3)$$

which are composed of P phased plane wave components with identical in-plane projection $k_{\parallel} = |\mathbf{k}_{\parallel}|$ and phases $\phi_j = (2\pi/P)j + \phi_0$ winding either counterclockwise ($\sigma = +1$) or clockwise ($\sigma = -1$). The constituent wave vectors for such an incident state are $\mathbf{k}_j^i = (k_{\parallel}^i \cos \phi_j, k_{\parallel}^i \sin \phi_j, k_z^i)$, with $k_i^2 = k_z^2 + k_{\parallel}^2$. For 60 keV probing electrons typical of STEM EEL spectroscopy, the plane waves contributing to the pinwheel superposition states require convergence angles of $\theta_c \sim 13.5$ mrad for k_{\parallel} at the hBN K/K' points, while relative phases may be imprinted using techniques to shape transverse free electron wave functions currently under development [46–50].

By preparing an incoming pinwheel state and post-selecting the on-axis plane wave state with $\mathbf{k}_{\parallel}^f = \mathbf{0}$, as depicted in Fig. 2a using a spatial filter in the Fourier plane, the measured inelastic scattering process will be composed of P phased momentum recoils with $\mathbf{q}_{j\parallel} = \mathbf{k}_{j\parallel}^i$, and the transition field has the form

$$\mathbf{E}_{P k_{\parallel} \sigma \phi_0, \mathbf{k} + \mathbf{G}}^0 = \frac{4\pi i e L}{L^3} \frac{\mathbf{k} + \mathbf{G}}{v_i} \frac{1}{|\mathbf{k} + \mathbf{G}|^2} \frac{1}{\sqrt{P}} \sum_{j=1}^P e^{i\phi_j} e^{i(\mathbf{k} + \mathbf{G}) \cdot (\mathbf{r}_\kappa - \mathbf{R}_0)} \delta_{\mathbf{k} + \mathbf{G}, \mathbf{q}_j}, \quad (4)$$

where \mathbf{R}_0 allows for the displacement of the transition field interference pattern in the xy plane relative to some arbitrarily placed origin. In close analogy to topological electromagnetic vortices created by interfering free space [4, 5] and evanescent [6–10] electromagnetic waves with controlled geometric phase, the in-plane polarization of the transition field $\mathbf{E}_{P k_{\parallel} \sigma \phi_0}^{0\parallel}(\mathbf{x})$ consists of a 2D periodic array of field vortices. The presently discussed topological field textures are distinguished from those previously reported in that the transition field is sourced by the charge density associated with the probing free electron transition, leading to field texture periodicity on the $\sim \text{\AA}$ length scale. For the case $P = 3$ and $k_{\parallel} = K, K'$, the phased momentum transfers have the same three-fold rotational reciprocal space symmetry as the K and K' phonons [12, 13], and the real space polarization array has hexagonal symmetry with unit cell dimensions matching those of the atomic crystal as presented in Fig. 2b for $\phi_0 = 0$. Superimposed above the 2D $|\mathbf{E}_{3k_{\parallel} \sigma \phi_0}^{0\parallel}(\mathbf{x}_{\parallel}, z = 0)|$ maps are polarization ellipses colored red (blue) to indicate anticlockwise (clockwise) polarization rotation. Reversing the winding direction of the plane wave phases by $\sigma = +1 \leftrightarrow \sigma = -1$ leads to a positional shift of the field nodes relative to the atomic crystal sites. The transition fields shown in Fig. 2b,c exhibit spin-momentum locking in the sense that simultaneous exchange of $\sigma = +1 \leftrightarrow \sigma = -1$ and $\phi_0 = 0 \leftrightarrow \phi_0 = \pi/3$, which is equivalent to $K \leftrightarrow K'$, yields the same spatial in-plane field intensity profile, with regions of clockwise and anticlockwise polarization rotation interchanged.

The ability of the identified free electron transitions to generate electric fields that mirror the spin texture and spin-momentum locking of the hBN chiral phonons makes it possible to leverage the former to directly probe the latter. Fig. 3a presents calculated transition rates $w_{\sigma}^{\phi_0}(\hbar\omega_{if}, \mathbf{R}_0)$ as a function of $\hbar\omega_{if}$ and ϕ_0 from Eq. (1) with $\mathbf{E}_{fi, \mathbf{k} + \mathbf{G}_{\kappa}}^0$ from Eq. (4) for transitions $|P = 3, k_{\parallel} = K, \sigma = \pm 1, \phi_0\rangle \rightarrow |\mathbf{k}_f^{\parallel} = 0\rangle$ with $\mathbf{R}_0 = -a_{\text{BN}}/2$. Red and blue traces correspond to $\sigma = +1$ and $\sigma = -1$, respectively. At this \mathbf{R}_0 and $\phi_0 = 0$, as depicted in Fig. 2b, the transition field either drives both sublattices equally with circular polarizations of opposite handedness ($\sigma = +1$), or the B sublattice is situated at a node of the driving field while the N sublattice is at an antinode of the circularly polarized driving field ($\sigma = -1$). Consequently, as can be rationalized from the real-space phonon mode motions depicted in Fig. 1c, only the modes at 119 meV and 141 meV appear in Fig. 3a for $\phi_0 = 0$, where each of the momentum recoils is associated with one of the three BZ K points. As ϕ_0 varies, the fixed-magnitude momentum recoils leave the BZ boundary and the features in the spectra shown in Fig. 3a evolve according to the hBN eigenmode dispersion along the circle of fixed k_{\parallel} . At $\phi_0 = \pi/3$, the momentum recoils are associated with the three BZ K' points, as shown in Fig. 2c, and the spectra in Fig. 3a are identical to those at $\phi_0 = 0$ with $\sigma = +1 \leftrightarrow \sigma = -1$ as anticipated from behavior of the phonon modes shown in Fig. 1c under $K \leftrightarrow K'$.

This signature of chiral phonon spin-momentum locking can be quantified by defining

$$\text{CD}_{\sigma}^{\phi_0}(\hbar\omega_{if}, \mathbf{R}_0) = 2 \frac{w_{+}^{\phi_0}(\hbar\omega_{if}, \mathbf{R}_0) - w_{-}^{\phi_0}(\hbar\omega_{if}, \mathbf{R}_0)}{\max[w_{+}^{\phi_0}(\hbar\omega_{if}, \mathbf{R}_0)] + \max[w_{-}^{\phi_0}(\hbar\omega_{if}, \mathbf{R}_0)]}, \quad (5)$$

where $\max[w_{\sigma}^{\phi_0}(\hbar\omega_{if}, \mathbf{R}_0)]$ denotes the maximum loss rate over all ϕ_0 values. For fixed \mathbf{R}_0 and ϕ_0 , $\text{CD}_{\sigma}^{\phi_0}(\hbar\omega_{if}, \mathbf{R}_0)$ quantifies the differential inelastic scattering rate associated with ± 1 units of PAM exchanged between the probing free electron and target at a given loss energy. The blue trace in Fig. 3b shows $\text{CD}_{\sigma}^{\phi_0}(\hbar\omega_{if}, \mathbf{R}_0 = -a_{\text{BN}}/2)$ for the hBN monolayer with $\phi_0 \in [0, \pi]$ and loss energy 119 meV. Mirroring the sublattice spin associated with the chiral phonon

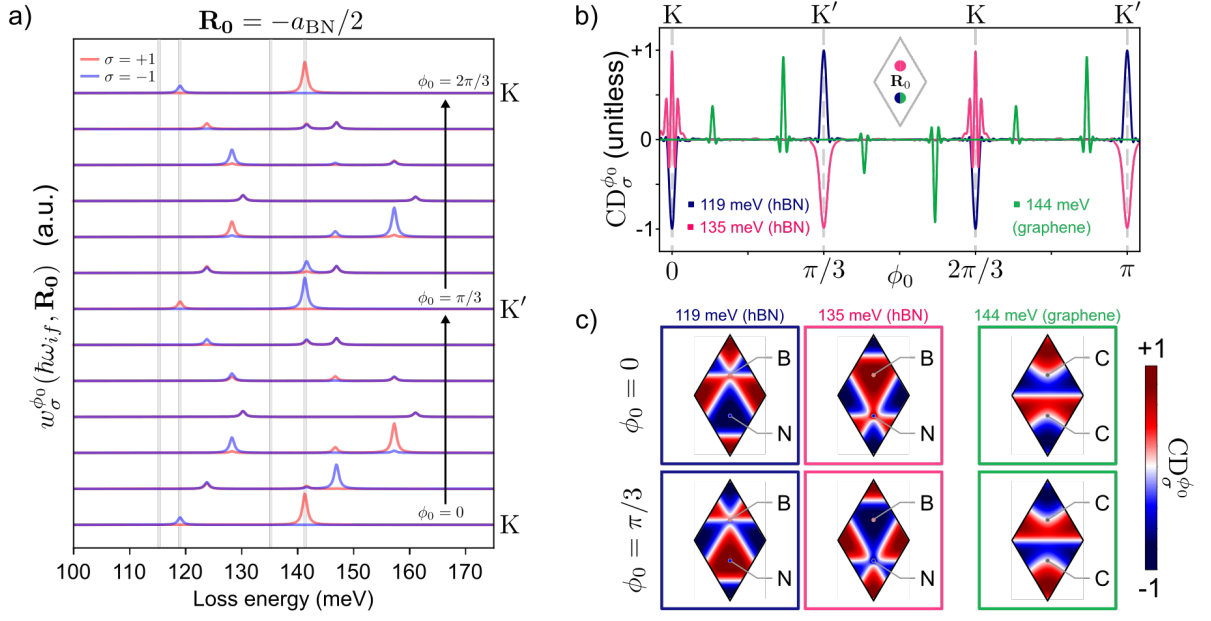


FIG. 3. Chiral phonon discrimination with phase shaped electrons. a) Calculated transition rates for incoming pinwheel states transitioning to the on-axis plane wave state as a function of loss energy and ϕ_0 for an hBN monolayer with $\mathbf{R}_0 = -a_{\text{BN}}/2$. Red (blue) traces indicate $\sigma = +1$ ($\sigma = -1$). b) Evolution of $CD_\sigma^{\phi_0}(\hbar\omega_\lambda)$ as a function of $\phi_0 \in [0, \pi]$ for selected loss energies and hBN and graphene targets. For hBN, $\mathbf{R}_0 = -a_{\text{BN}}/2$ for $\hbar\omega_\lambda = 111$ meV and $\mathbf{R}_0 = +a_{\text{BN}}/2$ for $\hbar\omega_\lambda = 135$ meV. $\mathbf{R}_0 = -a_{\text{CC}}/2$ for the graphene mode at $\hbar\omega_\lambda = 144$ meV. c) Spatial maps of $CD_\sigma^{\phi_0}(\hbar\omega_{if}, \mathbf{R}_0)$ for 119 meV (hBN), 135 meV (hBN), and 144 meV (graphene) with $\phi_0 = 0$ (upper) and $\phi_0 = \pi/3$ (lower), and \mathbf{R}_0 varied throughout the unit cell. All calculations include an empirical damping rate of $\eta = 1$ meV/ \hbar at zero temperature and a vacuum background.

[12], $CD_\sigma^{\phi_0} \sim 0$, except where $CD_\sigma^{\phi_0} = \pm 1$ at $\phi_0 = m(\pi/3)$ ($m \in \mathbb{Z}$) due to complete suppression of loss rates for either $\sigma = \pm 1$ at these ϕ_0 values. This behavior, evident also in Fig. 3a, is a consequence of PAM conservation during the inelastic scattering process [12, 27]. Since $|P = 3, k_\parallel, \sigma = \pm 1, \phi_0\rangle \rightarrow |\mathbf{k}_f^\parallel = \mathbf{0}\rangle$ is associated with $\Delta\text{PAM} = -\sigma$, these transitions couple only to phonons with $\text{PAM} = +\sigma$. The spin-momentum locking of the hBN phonon modes exhibited in Fig. 1c under $K \leftrightarrow K'$, therefore, underlies the sign change of $CD_\sigma^{\phi_0=m(\pi/3)}$ in Fig. 3b as a function of m .

Similarly, when $\mathbf{R}_0 = +a_{\text{BN}}/2$, the transition field profiles in Figs. 2b,c are shifted vertically upwards relative to the fixed atomic sites such that the N sublattice sites reside at nodes of the transition field, while the B sites reside at antinodes of $\mathbf{E}_{3k_\parallel\sigma\phi_0}^{0\parallel}(\mathbf{x})$ with circular polarization states for $\sigma = +1$ and $\phi_0 = 0$ [64]. This transition field couples to the K/K' phonon modes at 135 meV (pink trace) associated with precession of the B sublattice sites (Fig. 1c). The opposite sign of the PAM associated with the 119 meV and 135 meV modes at both K and K' result in the opposite signs of $CD_\sigma^{\phi_0=m(\pi/3)}$ for these two loss energies at each m as shown in Fig. 3b. Unlike in hBN where the lack of spatial inversion symmetry leads to the non-degenerate K/K' phonons with $\text{PAM} = \pm 1\hbar$ at 119 meV and 135 meV, spatial inversion symmetry in graphene leads to the degeneracy of the phonon modes associated with circular motion on either sublattice at K/K', and a net $\text{PAM} = 0\hbar$ at $\hbar\omega_{if} = 144$ meV (see SM [64]). Therefore, as a point of comparison, Fig. 3b includes $CD_\sigma^{\phi_0}(\hbar\omega_{if} = 144 \text{ meV}, \mathbf{R}_0 = -a_{\text{CC}}/2)$ for a graphene monolayer (green trace). As anticipated based upon the PAM conservation argument invoked above, $CD_\sigma^{\phi_0=m(\pi/3)} = 0$ for graphene at 144 meV as depicted in Fig. 3b. See SM [64] for additional results pertaining to the evolution of $CD_\sigma^{\phi_0}$ for hBN and graphene.

In contrast to the optical techniques previously employed to measure chiral phonons, atomic scale spatial information

regarding sublattice spin can be accessed using the proposed inelastic free electron scattering strategy. Varying \mathbf{R}_0 , e.g., by spatially translating the (monolayer) sample relative to the fixed widefield periodic array of transition field vortices, allows the various local in-plane polarization states of the $\mathbf{E}_{3k_{\parallel}\sigma\phi_0}^{0\parallel}(\mathbf{x})$ site-space unit cell to be scanned across the atomic positions, modulating the electron-chiral-phonon coupling. We emphasize that the proposed detection scheme does not require careful a priori alignment of the transition field relative to the atomic crystal sites. Instead, it is required that the sign of $\sigma = \pm 1$ can be reversed keeping \mathbf{R}_0 fixed such that $\text{CD}_{\sigma}^{\phi_0}(\hbar\omega_{if}, \mathbf{R}_0)$ is well defined. Spatial maps of $\text{CD}_{\sigma}^{\phi_0}(\hbar\omega_{if}, \mathbf{R}_0)$ are presented in Fig. 3c for the hBN and graphene K/K' modes considered in Fig. 3b, while other in-plane modes are presented in the SM [64]. In the case of hBN, the spatial maps clearly reflect the spatial inversion symmetry breaking and the localization of the sublattice spin (phonon motion) onto one or the other sublattices as exhibited in Fig. 1c. The spatial maps of $\text{CD}_{\sigma}^{\phi_0}(\hbar\omega_{if} = 144 \text{ meV}, \mathbf{R}_0)$ for graphene are odd with respect to y reflection due to spatial inversion symmetry. The ability of this inelastic electron scattering strategy to encode Å-scale spatial information directly related to the rotational motion of the sublattice sites constitutes a significant advantage over previous chiral phonon characterization techniques.

Chiral phonons with valley pseudospin degrees of freedom and well-defined PAM underlie a diversity of fundamental condensed matter physics phenomena, material properties, and downstream technologies exploiting unidirectional and lossless phonon propagation in the infrared. However, direct characterization of chiral phonons has remained an outstanding challenge [27] owing to the small linear momentum of light and the absence of obvious polarization degrees of freedom of massive particles. Here we show how pre- and post-selection of pinwheel free electron states during inelastic scattering overcomes these limitations and introduces a new PAM degree of freedom enabling tracking of PAM exchange between probe and sample. By tailoring such pinwheel states to generate 2D periodic arrays of in-plane field vortices with Å-scale polarization textures, we introduce a strategy for direct and selective detection of phonon spin textures of the desired chiral mode symmetries at the K/K' valleys using phase-structured free electrons. Other material systems hosting chiral phonons with various composition, symmetry, and dimensionality could be characterized using generalizations of the proposed inelastic scattering measurements.

All work was supported by the U.S. Department of Energy (DOE), Office of Science, Office of Basic Energy Sciences (BES), Materials Sciences and Engineering Division under Award No. DOE BES DE-SC0022921.

* masiello@uw.edu

- [1] K. Inomata and M. Kamionkowski, Chiral photons from chiral gravitational waves, *Phys. Rev. Lett.* **123**, 031305 (2019).
- [2] U. Al Khawaja and H. Stoof, Skyrmions in a ferromagnetic Bose-Einstein condensate, *Nature* **411**, 918 (2001).
- [3] X. Yu, W. Koshibae, Y. Tokunaga, K. Shibata, Y. Taguchi, N. Nagaosa, and Y. Tokura, Transformation between meron and skyrmion topological spin textures in a chiral magnet, *Nature* **564**, 95 (2018).
- [4] S. Gao, F. C. Speirits, F. Castellucci, S. Franke-Arnold, S. M. Barnett, and J. B. Götte, Paraxial skyrmionic beams, *Phys. Rev. A* **102**, 053513 (2020).
- [5] Y. Shen, Y. Hou, N. Papasimakis, and N. I. Zheludev, Supertoroidal light pulses as electromagnetic skyrmions propagating in free space, *Nat. Commun.* **12**, 5891 (2021).
- [6] S. Tsesses, E. Ostrovsky, K. Cohen, B. Gjonaj, N. Lindner, and G. Bartal, Optical skyrmion lattice in evanescent electro-

magnetic fields, *Science* **361**, 993 (2018).

- [7] L. Du, A. Yang, A. V. Zayats, and X. Yuan, Deep-subwavelength features of photonic skyrmions in a confined electromagnetic field with orbital angular momentum, *Nat. Phys.* **15**, 650 (2019).
- [8] Y. Dai, Z. Zhou, A. Ghosh, R. S. Mong, A. Kubo, C.-B. Huang, and H. Petek, Plasmonic topological quasiparticle on the nanometre and femtosecond scales, *Nature* **588**, 616 (2020).
- [9] T. J. Davis, D. Janoschka, P. Dreher, B. Frank, F.-J. Meyer zu Heringdorf, and H. Giessen, Ultrafast vector imaging of plasmonic skyrmion dynamics with deep subwavelength resolution, *Science* **368**, eaba6415 (2020).
- [10] A. Ghosh, S. Yang, Y. Dai, and H. Petek, The spin texture topology of polygonal plasmon fields, *ACS Photonics* **10**, 13 (2023).
- [11] S.-Y. Chen, C. Zheng, M. S. Fuhrer, and J. Yan, Helicity-resolved Raman scattering of MoS₂, MoSe₂, WS₂, and WSe₂ atomic layers, *Nano Lett.* **15**, 2526 (2015).
- [12] L. Zhang and Q. Niu, Chiral phonons at high-symmetry points in monolayer hexagonal lattices, *Phys. Rev. Lett.* **115**, 115502 (2015).
- [13] H. Zhu, J. Yi, M.-Y. Li, J. Xiao, L. Zhang, C.-W. Yang, R. A. Kaindl, L.-J. Li, Y. Wang, and X. Zhang, Observation of chiral phonons, *Science* **359**, 579 (2018).
- [14] H. Chen, W. Zhang, Q. Niu, and L. Zhang, Chiral phonons in two-dimensional materials, *2D Mater.* **6**, 012002 (2018).
- [15] H. Chen, W. Wu, S. A. Yang, X. Li, and L. Zhang, Chiral phonons in kagome lattices, *Phys. Rev. B* **100**, 094303 (2019).
- [16] N. Suri, C. Wang, Y. Zhang, and D. Xiao, Chiral phonons in moiré superlattices, *Nano Lett.* **21**, 10026 (2021).
- [17] Q. Wang, S. Li, J. Zhu, H. Chen, W. Wu, W. Gao, L. Zhang, and S. A. Yang, Chiral phonons in lattices with C₄ symmetry, *Phys. Rev. B* **105**, 104301 (2022).
- [18] T. Zhang and S. Murakami, Chiral phonons and pseudoangular momentum in nonsymmorphic systems, *Phys. Rev. Research* **4**, L012024 (2022).
- [19] J. Fransson, Chiral phonon induced spin polarization, *Phys. Rev. Research* **5**, L022039 (2023).
- [20] H. Chen, W. Wu, J. Zhu, S. A. Yang, and L. Zhang, Propagating chiral phonons in three-dimensional materials, *Nano Lett.* **21**, 3060 (2021).
- [21] K. Ishito, H. Mao, Y. Kousaka, Y. Togawa, S. Iwasaki, T. Zhang, S. Murakami, J.-i. Kishine, and T. Satoh, Truly chiral phonons in α -HgS, *Nat. Phys.* **19**, 35 (2023).
- [22] H. Ueda, M. García-Fernández, S. Agrestini, C. P. Romao, J. van den Brink, N. A. Spaldin, K.-J. Zhou, and U. Staub, Chiral phonons in quartz probed by x-rays, *Nature*, 1 (2023).
- [23] G. Grissonnanche, S. Thériault, A. Gourgout, M.-E. Boulanger, E. Lefrançois, A. Ataei, F. Laliberté, M. Dion, J.-S. Zhou, S. Pyon, T. Takayama, H. Takagi, N. Doiron-Leyraud, and L. Taillefer, Chiral phonons in the pseudogap phase of cuprates, *Nat. Phys.* **16**, 1108 (2020).
- [24] K. Kim, E. Vetter, L. Yan, C. Yang, Z. Wang, R. Sun, Y. Yang, A. H. Comstock, X. Li, J. Zhou, L. Zhang, W. You, D. Sun, and J. Liu, Chiral-phonon-activated spin Seebeck effect, *Nat. Mater.* **22**, 322 (2023).
- [25] S. G. Jeong, J. Kim, A. Seo, S. Park, H. Y. Jeong, Y.-M. Kim, V. Lauter, T. Egami, J. H. Han, and W. S. Choi, Unconventional interlayer exchange coupling via chiral phonons in synthetic magnetic oxide heterostructures, *Sci. Adv.* **8**, eabm4005 (2022).
- [26] H. Chen, W. Wu, J. Zhu, Z. Yang, W. Gong, W. Gao, S. A. Yang, and L. Zhang, Chiral phonon diode effect in chiral crystals, *Nano Lett.* **22**, 1688 (2022).
- [27] T. Wang, H. Sun, X. Li, and L. Zhang, Chiral phonons: Prediction, verification, and application, *Nano Lett.* **24**, 4311 (2024).
- [28] O. L. Krivanek, T. C. Lovejoy, N. Dellby, T. Aoki, R. Carpenter, P. Rez, E. Soignard, J. Zhu, P. E. Batson, M. J. Lagos, R. F. Egerton, and P. A. Crozier, Vibrational spectroscopy in the electron microscope, *Nature* **514**, 209 (2014).

- [29] C. Dwyer, T. Aoki, P. Rez, S. Chang, T. Lovejoy, and O. Krivanek, Electron-beam mapping of vibrational modes with nanometer spatial resolution, *Phys. Rev. Lett.* **117**, 256101 (2016).
- [30] M. J. Lagos, A. Trügler, U. Hohenester, and P. E. Batson, Mapping vibrational surface and bulk modes in a single nanocube, *Nature* **543**, 529 (2017).
- [31] F. S. Hage, R. J. Nicholls, J. R. Yates, D. G. McCulloch, T. C. Lovejoy, N. Dellby, O. L. Krivanek, K. Refson, and Q. M. Ramasse, Nanoscale momentum-resolved vibrational spectroscopy, *Sci. Adv.* **4**, eaar7495 (2018).
- [32] J. A. Hachtel, J. Huang, I. Popovs, S. Jansone-Popova, J. K. Keum, J. Jakowski, T. C. Lovejoy, N. Dellby, O. L. Krivanek, and J. C. Idrobo, Identification of site-specific isotopic labels by vibrational spectroscopy in the electron microscope, *Science* **363**, 525 (2019).
- [33] R. Senga, K. Suenaga, P. Barone, S. Morishita, F. Mauri, and T. Pichler, Position and momentum mapping of vibrations in graphene nanostructures, *Nature* **573**, 247 (2019).
- [34] J. Hong, R. Senga, T. Pichler, and K. Suenaga, Probing exciton dispersions of freestanding monolayer wse 2 by momentum-resolved electron energy-loss spectroscopy, *Phys. Rev. Lett.* **124**, 087401 (2020).
- [35] A. O'Hara, B. Plotkin-Swing, N. Dellby, J. C. Idrobo, O. L. Krivanek, T. C. Lovejoy, and S. T. Pantelides, High-temperature phonons in h-BN: momentum-resolved vibrational spectroscopy and theory, arXiv preprint arXiv:2310.13813 (2023).
- [36] J. Li, J. Li, J. Tang, Z. Tao, S. Xue, J. Liu, H. Peng, X.-Q. Chen, J. Guo, and X. Zhu, Direct observation of topological phonons in graphene, *Phys. Rev. Lett.* **131**, 116602 (2023).
- [37] J. Li, L. Wang, Y. Wang, Z. Tao, W. Zhong, Z. Su, S. Xue, G. Miao, W. Wang, H. Peng, J. Guo, and X. Zhu, Observation of the nonanalytic behavior of optical phonons in monolayer hexagonal boron nitride, *Nat. Commun.* **15**, 1938 (2024).
- [38] J. Yuan and N. K. Menon, Magnetic linear dichroism in electron energy loss spectroscopy, *J. Appl. Phys.* **81**, 5087 (1997).
- [39] C. Hébert and P. Schattschneider, A proposal for dichroic experiments in the electron microscope, *Ultramicroscopy* **96**, 463 (2003).
- [40] P. Schattschneider, S. Rubino, C. Hébert, J. Rusz, J. Kuneš, P. Novák, E. Carlino, M. Fabrizioli, G. Panaccione, and G. Rossi, Detection of magnetic circular dichroism using a transmission electron microscope, *Nature* **441**, 486 (2006).
- [41] G. Guzzinati, A. Béch  , H. Louren  o-Martins, J. Martin, M. Kociak, and J. Verbeeck, Probing the symmetry of the potential of localized surface plasmon resonances with phase-shaped electron beams, *Nat. Commun.* **8**, 1 (2017).
- [42] A. Asenjo-Garcia and F. J. Garc  a de Abajo, Dichroism in the interaction between vortex electron beams, plasmons, and molecules, *Phys. Rev. Lett.* **113**, 066102 (2014).
- [43] M. Zanfrognini, E. Rotunno, S. Frabboni, A. Sit, E. Karimi, U. Hohenester, and V. Grillo, Orbital angular momentum and energy loss characterization of plasmonic excitations in metallic nanostructures in TEM, *ACS Photonics* **6**, 620 (2019).
- [44] H. Louren  o-Martins, D. G  rard, and M. Kociak, Optical polarization analogue in free electron beams, *Nat. Phys.* **17**, 598 (2021).
- [45] M. R. Bourgeois, A. G. Nixon, M. Chalifour, and D. J. Masiello, Optical polarization analogs in inelastic free-electron scattering, *Sci. Adv.* **9**, eadj6038 (2023).
- [46] C.-P. Yu, F. Vega Iba  ez, A. B  ch  , and J. Verbeeck, Quantum wavefront shaping with a 48-element programmable phase plate for electrons, *SciPost Phys.* **15**, 223 (2023).
- [47] A. Feist, S. V. Yalunin, S. Sch  fer, and C. Ropers, High-purity free-electron momentum states prepared by three-dimensional optical phase modulation, *Phys. Rev. Res.* **2**, 043227 (2020).
- [48] I. Madan, V. Leccese, A. Mazur, F. Barantani, T. LaGrange, A. Sapozhnik, P. M. Tengdin, S. Gargiulo, E. Rotunno, J.-C. Olaya, I. Kaminer, V. Grillo, F. J. Garc  a de Abajo, F. Carbone, and G. M. Vanacore, Ultrafast transverse modulation of free electrons by interaction with shaped optical fields, *ACS Photonics* **9**, 3215 (2022).
- [49] T. R. Harvey, J. S. Pierce, A. K. Agrawal, P. Ercius, M. Linck, and B. J. McMorran, Efficient diffractive phase optics for electrons, *New J. Phys.* **16**, 093039 (2014).

- [50] S. Tsesses, R. Dahan, K. Wang, T. Bucher, K. Cohen, O. Reinhardt, G. Bartal, and I. Kaminer, Tunable photon-induced spatial modulation of free electrons, *Nat. Mater.* **22**, 345 (2023).
- [51] S. Lloyd, M. Babiker, and J. Yuan, Quantized orbital angular momentum transfer and magnetic dichroism in the interaction of electron vortices with matter, *Phys. Rev. Lett.* **108**, 074802 (2012).
- [52] W. Cai, O. Reinhardt, I. Kaminer, and F. J. García de Abajo, Efficient orbital angular momentum transfer between plasmons and free electrons, *Phys. Rev. B* **98**, 045424 (2018).
- [53] M. R. Bourgeois, A. G. Nixon, M. Chalifour, E. K. Beutler, and D. J. Masiello, Polarization-resolved electron energy gain nanospectroscopy with phase-structured electron beams, *Nano Lett.* **22**, 7158 (2022).
- [54] M. T. Dove, *Introduction to Lattice Dynamics* (Cambridge University Press, 1993).
- [55] A. Bosak, M. Krisch, M. Mohr, J. Maultzsch, and C. Thomsen, Elasticity of single-crystalline graphite: Inelastic x-ray scattering study, *Phys. Rev. B* **75**, 153408 (2007).
- [56] K. Michel and B. Verberck, Theory of the evolution of phonon spectra and elastic constants from graphene to graphite, *Phys. Rev. B* **78**, 085424 (2008).
- [57] K. Michel and B. Verberck, Theory of elastic and piezoelectric effects in two-dimensional hexagonal boron nitride, *Phys. Rev. B* **80**, 224301 (2009).
- [58] U. Hohenester, A. Trügler, P. E. Batson, and M. J. Lagos, Inelastic vibrational bulk and surface losses of swift electrons in ionic nanostructures, *Phys. Rev. B* **97**, 165418 (2018).
- [59] J. J. Sakurai, *Modern Quantum Mechanics* (Benjamin/Cummings Publishing Company, 1985).
- [60] A. W. Rossi, M. R. Bourgeois, C. Walton, and D. J. Masiello, Probing the polarization of low-energy excitations in 2d materials from atomic crystals to nanophotonic arrays using momentum-resolved electron energy loss spectroscopy, *arXiv preprint arXiv:2402.04481* (2024).
- [61] M. Uchida and A. Tonomura, Generation of electron beams carrying orbital angular momentum, *Nature* **464**, 737 (2010).
- [62] J. Verbeeck, H. Tian, and P. Schattschneider, Production and application of electron vortex beams, *Nature* **467**, 301 (2010).
- [63] K. Y. Bliokh, I. P. Ivanov, G. Guzzinati, L. Clark, R. Van Boxem, A. Béch  , R. Juchtmans, M. A. Alonso, P. Schattschneider, F. Nori, and J. Verbeeck, Theory and applications of free-electron vortex states, *Phys. Rep.* **690**, 1 (2017).
- [64] Supplemental Material at [url] includes a description of the employed hBN and graphene phonon models as well as additional state- and energy-resolved loss rate calculations.